Spatially-resolved in-situ/operando structural study of screen-printed BaTiO3/P(VDF-TrFE) flexible piezoelectric device

Christine Revenant, Sylvain Minot, Simon Toinet, Eleanor Lawrence Bright, Raphaël Ramos, Mohammed Benwadih

Sensors & Actuators: A. Physical 377 (2024) 115738

Contents lists available at ScienceDirect

Sensors and Actuators: A. Physical

journal homepage: www.journals.elsevier.com/sensors-and-actuators-a-physical

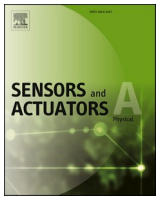

Spatially-resolved in-situ/operando structural study of screen-printed $BaTiO_3$/P(VDF-TrFE) flexible piezoelectric device

Christine Revenant [a,*], Sylvain Minot [b], Simon Toinet [b], Eleanor Lawrence Bright [c], Raphaël Ramos [b], Mohammed Benwadih [b]

[a] Univ. Grenoble Alpes, CEA, IRIG-MEM, NRX, Grenoble 38000, France
[b] Univ. Grenoble Alpes, CEA, LITEN/DTNM, Grenoble 38000, France
[c] European Synchrotron Radiation Facility, Grenoble, France

ARTICLE INFO

Keywords:
Screen printing
Polymer
Ceramic
Surfactant
Piezoelectric

ABSTRACT

The incorporation of lead-free $BaTiO_3$ particles into P(VDF-TrFE) provides a versatile way for tuning dielectric and piezoelectric properties. Screen-printing enables the easy production of flexible capacitors. To prevent particle aggregation, the $BaTiO_3$ particles are functionalized with a surfactant. Initially, 60 % vol. $BaTiO_3$ particles are deposited in the second layer out of three layers. After annealing and cooling, the particle distribution is successfully homogeneous in the whole film. After poling at 80 °C, the relative permittivity and the piezoelectric coefficient d_{33} significantly increase up to 159 and 8 pC/N respectively. In situ/operando spatially-resolved X-ray techniques allow exploring the structural evolution of the composite device during annealing and during an applied electric field. The application of an electric field leads to the quasi-disappearance of the P(VDF-TrFE) ferroelectric state. As a matter of fact, the interactions between the P(VDF-TrFE) and the surfactant may limit the rotation of P(VDF-TrFE) chains near the particles. Hence, paraelectric polymers could be chosen on a mechanical or economic basis for the matrix in piezoelectric composite devices. Regarding $BaTiO_3$, the lattice strain evolves from an extrinsic strain at RT to an intrinsic strain after annealing and cooling. At the cooled state, the tetragonality c/a is higher than 1.01, leading to improved piezoelectric properties. The increase of the average domain size leads to the increase of the composite permittivity. Finally this knowledge facilitates the development of tailored flexible piezoelectric composite devices.

1. Introduction

Composite materials are increasingly studied due to their diverse properties leading to various applications, such as cathodes for batteries [1,2], coatings [3,4], electromagnetic interference shielding film [5], microspheres for artificial photosynthesis [6], photodetectors [7,8], and gas sensors [9].

Lead-free $BaTiO_3$ is a well-used polycrystalline ceramic, which is paraelectric (resp. ferroelectric) in case of a cubic (resp. tetragonal) lattice [10]. With the application of an electric field, the deformations can originate from the intrinsic strain of the lattice, induced by piezoelectric effects, and the extrinsic strain, on a length scale larger than a unit cell, originating from the motion of the boundary between two domains, called a domain wall (DW). The DWs are characterized by the angle of polarization axes between two adjacent domains, such as 180° and 90° DWs [11], existing in a tetragonal phase of $BaTiO_3$ [12]. After the removal of the electric field, the DW movement is irreversible, as the induced strain. Unfortunately, the poor flexibility of $BaTiO_3$ limits applications for large-scale fabrication, flexible devices, and deposition on 3D surfaces. Hence, $BaTiO_3$ particles have been mixed with polymers, like the semicrystalline polyvinylidene fluoride trifluoroethylene P (VDF-TrFE) copolymer. Flexible $BaTiO_3$/PVDF based capacitors are used as actuators, sensors [13], and energy storage devices [14,15]. Among the different crystalline forms of P(VDF-TrFE), the β phase is ferroelectric, whereas the α phase is paraelectric [16]. The ceramics exhibit significantly higher dielectric properties compared to pure P (VDF-TrFE). The dielectric constant of $BaTiO_3$ is maximum for grain sizes near 1 μm, namely 5000 for grain sizes ranging from 0.7 to 1 μm [17]. On the contrary, the dielectric constant of P(VDF-TrFE) is very low, approximately 10 [18,19]. These contrasting permittivity values make these materials promising candidates for applications requiring high dielectric properties.

* Corresponding author.
E-mail address: christine.revenant@cea.fr (C. Revenant).

https://doi.org/10.1016/j.sna.2024.115738
Received 23 May 2024; Received in revised form 5 July 2024; Accepted 22 July 2024
Available online 23 July 2024

The screen-printing technique is increasingly used for depositing thin films due to its quick, easy, low-cost nature, and the possibility of depositing on plastic substrates in order to obtain flexible devices [20,21]. This technique was recently used to deposit films of $BaTiO_3$/P(VDF-TrFE) [22]. Due to the high surface energy of $BaTiO_3$ particles, the particles can agglomerate in PVDF based films. Heterogeneous dispersion and porosity weaken dielectric and piezoelectric properties, as well as mechanical strength. In order to prevent particles from agglomeration in the polymeric matrix, particles are coated with a surfactant. With traditional deposition methods, $BaTiO_3$ particles are found much more at the bottom than at the top of PVDF based films [23]. Moreover, P(VDF-TrFE) films with a high percentage of $BaTiO_3$ can have a rough surface. In order to avoid these two drawbacks, an innovative deposition method is tried i.e. 60 % vol. particles are deposited only in the second layer out of three layers. The third deposited layer made of P(VDF-TrFE) fills the gaps between the particles and yields a smooth surface. After the deposition, annealing may lead to a homogeneous distribution of the particles. Regarding the material properties, a significant increase in both permittivity and piezoelectricity is obtained after high-temperature poling [22].

Optimizing the performance of the printed materials is a key issue. To start with, the homogeneous distribution of the particles has to be assessed after the elaboration process. Then the structure of the polymer and of the particles has to be determined during annealing and during the application of an electric field, similarly to what happens during poling. Finally the correlation structure/property has to be clearly established in order to optimize further the capacitor performance. In situ/operando High Resolution X-Ray Diffraction (HRXRD) [24,25] and simultaneous fluorescence spectromicrography were used to study the structure evolution of the capacitors as a function of the film depth. Transmission HRXRD performed with a submicrometer synchrotron radiation X-ray beam allows probing regions successively in the top electrode, the active layer, the bottom electrode, and the substrate. The uniqueness of this study consists in using high quality transmission HRXRD through the capacitor, from top to bottom, with a submicrometer X-ray beam and without any substrate background. This allows addressing the structural evolution of the particles and of the polymer as a function of the film depth, annealing, and the applied electric field. We think that the combination of HRXRD/fluorescence/Fourier Transform InfraRed spectroscopy (FTIR) studies could explain the significant changes in both permittivity and piezoelectricity as a function of thermal states.

In this study, the dielectric and piezoelectric properties are presented as a function of the amount of $BaTiO_3$. The structure of the $BaTiO_3$/P(VDF-TrFE) capacitor is then studied as a function of annealing and of the applied electric field, before being correlated to the dielectric and piezoelectric properties.

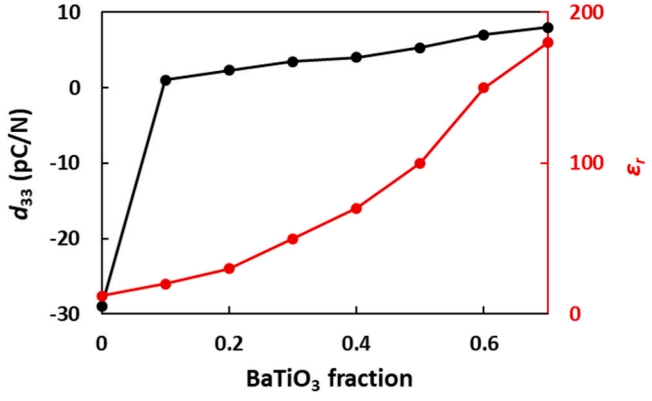

Fig. 1. Relative permittivity ε_r at 10 kHz and piezoelectric coefficient d_{33} of the composites after poling at 80 °C as a function of the $BaTiO_3$ fraction up to 0.7, near the densest close-packing of equal spheres.

2. Experimental section

2.1. Materials

The polyimide (PI) substrate (25 μm) was washed with acetone and propanol. The substrate was then exposed to a UV lamp during 1 min. In order to ensure a good adhesiveness of the screen-printed material, a fluorinated treatment (SF_6 plasma) was made on the substrate. The electrodes were made of CLEVIOS™ S V4 STAB poly(3,4-ethylenedioxythiophene) polystyrene sulfonate (PEDOT:PSS) synthesized by Heraeus. A PEDOT:PSS electrode was deposited with an EKRA® X5-STS (Global BizTeK Co., Gyeonggido, South Korea) screen-printer on the substrate. To perform solvent evaporation, each layer was annealed on a heating plate. The electrode was annealed at 150 °C during 25 min. A fluorinated treatment (SF_6 plasma) was also made on the electrode. We used the FC20P grade of P(VDF-TrFE) (80–20) synthesized by ARKEMA-Piezotech. The solvent used to dissolve P(VDF-TrFE) is triethyl phosphate (TEP). Commercial $BaTiO_3$ powder from Sigma Aldrich® (Darmstadt, Germany) was used. The average particle diameter was less than 1 μm. The $BaTiO_3$ particles were functionalized with the 3-Fluoro-4-(trifluoromethyl)benzoic acid surfactant called 3 F-met. The functionalized particles and the polymer solution were added, gradually and alternatively, into a mixer (Heidolph, RZR 2020, Germany). Mixing was performed at 1500 rpm during 1.25 h. The $BaTiO_3$/P(VDF-TrFE) samples were fabricated by screen-printing on PEDOT:PSS with three deposition steps. The first and third deposits consisted only of P(VDF-TrFE) and the second one consisted of P(VDF-TrFE) with 60 % vol. of $BaTiO_3$. Between each deposited layer, a partial solvent evaporation was made at 150 °C during 5 min. After the composite film deposition, a solvent evaporation was performed at 150 °C during 2 hours. Fig. S1 shows Scanning Electron Microscope (SEM) views of the particles without/with surfactant. Finally the 19-μm thick film is sandwiched between two PEDOT:PSS electrodes, each with a thickness of 1 μm [22]. The contacts with the device were realized with an Ag-paste (EMS CI-1001, Nagase Engineered Materials Systems Inc., USA) characterized by an electrical resistance smaller than 15 mΩ.

2.2. Characterization

The relative permittivity ε_r was obtained with the relation [26]:

$$C = \frac{\varepsilon_0 \varepsilon_r S}{d} \quad (1)$$

Here, C is the device capacitance, ε_0 the vacuum permittivity, S the capacitance area, d the film thickness. Measurements were performed with an Agilent E4980A LCR meter under an AC voltage level of 1 V.

The piezoelectric coefficient d_{33} was measured with a setup composed of a dynamic oscillator (PI 246–50) coupled with a waveform generator (33522B, Keysight Technologies Inc., Santa Rosa, CA, USA) together with a voltage amplifier (Model 20/20 C, TREK Inc., Novi, MI, USA). This enables generating a sinusoidal force with a tunable amplitude and frequency. The setup comprised also a C11 force sensor (HBM, Darmstadt, Germany) and a charge sensor (KISTLER, Type 5015, Winterthur, Switzerland). The measurements were performed at a frequency of 1 Hz, with a force amplitude of about 700 N and a bias of 70–100 N. Finally real-time signals were simultaneously recorded using DEWE platform (Sirius, 8XSGT, SI-1420 Trbovlje, Slovenia). Here, C_{PP} and F_{PP} are respectively the peak-to-peak charge and force amplitudes, A_C is the area on which the charge accumulates, and A_F is the area on which the force is applied. The piezoelectric charge coefficient d_{33} is determined by [27]:

$$d_{33} = (C_{PP} / A_C) / (F_{PP} / A_F) \quad (2)$$

The large-scale homogeneity of screen-printing was tested. Devices originating from different locations of a screen-printed sheet yielded

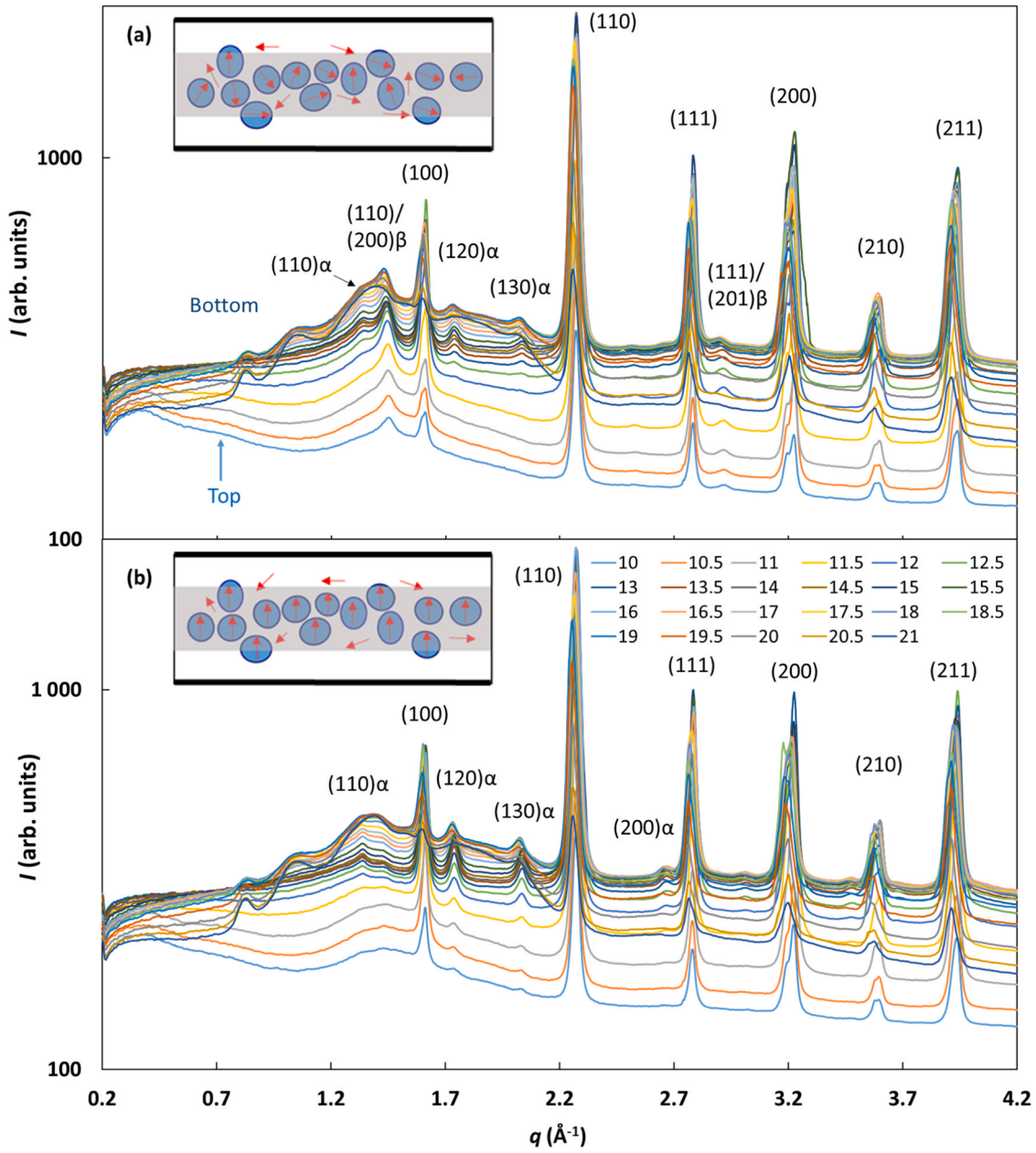

Fig. 2. HRXRD patterns of the composite film collected at RT during the vertical scan of the sample from top to bottom at (a) 0 V/μm and (b) 3.15 V/μm. Inset: Schematic of the composite capacitor with the inorganic particles in the center of the organic matrix. (a) Prior to the application of an electric field, the distribution of the dipoles is random in the copolymer and in the particles. (b) With the application of an electric field, the dipoles are oriented only in the particles. The presented HRXRD measurements correspond only to the region with $BaTiO_3$ particles (in grey) from 10 to 21 μm of the support translation. The intensity is on a log scale. All the referenced peaks correspond to $BaTiO_3$ except the α and β peaks.

similar relative permittivity and piezoelectric coefficient values (Fig. S2).

The HRXRD method is described in the Supplementary Information (Fig. S3).

Infrared (IR) spectroscopy reflectance spectra were recorded over the spectral range 500 – 4000 cm^{-1} with 128 scans and the spectral resolution of these measurements was ± 4 cm^{-1}. IR measurements were performed on a Bruker IFS55 Fourier transform spectrometer using a reflective Cassegrain microscope objective.

3. Results and discussion

3.1. Dielectric and piezoelectric properties

Before poling, the composite capacitor is not piezoelectric. Fig. 1 shows the evolution of the relative permittivity and of the piezoelectric coefficient of the composites after poling at 80 °C as a function of the $BaTiO_3$ fraction.

The relative permittivity of pure P(VDF-TrFE) is 12, similar to the values of 10 for PVDF at 10 Hz [28] and 16 for P(VDF-TrFE) at 100 Hz [19]. When the percentage of $BaTiO_3$ increases, the relative permittivity also increases, in agreement with a study conducted on PVDF with a low percentage of $BaTiO_3$ [28]. At 60 % $BaTiO_3$, the relative permittivity reaches 159, which is larger than the previous values in the range of

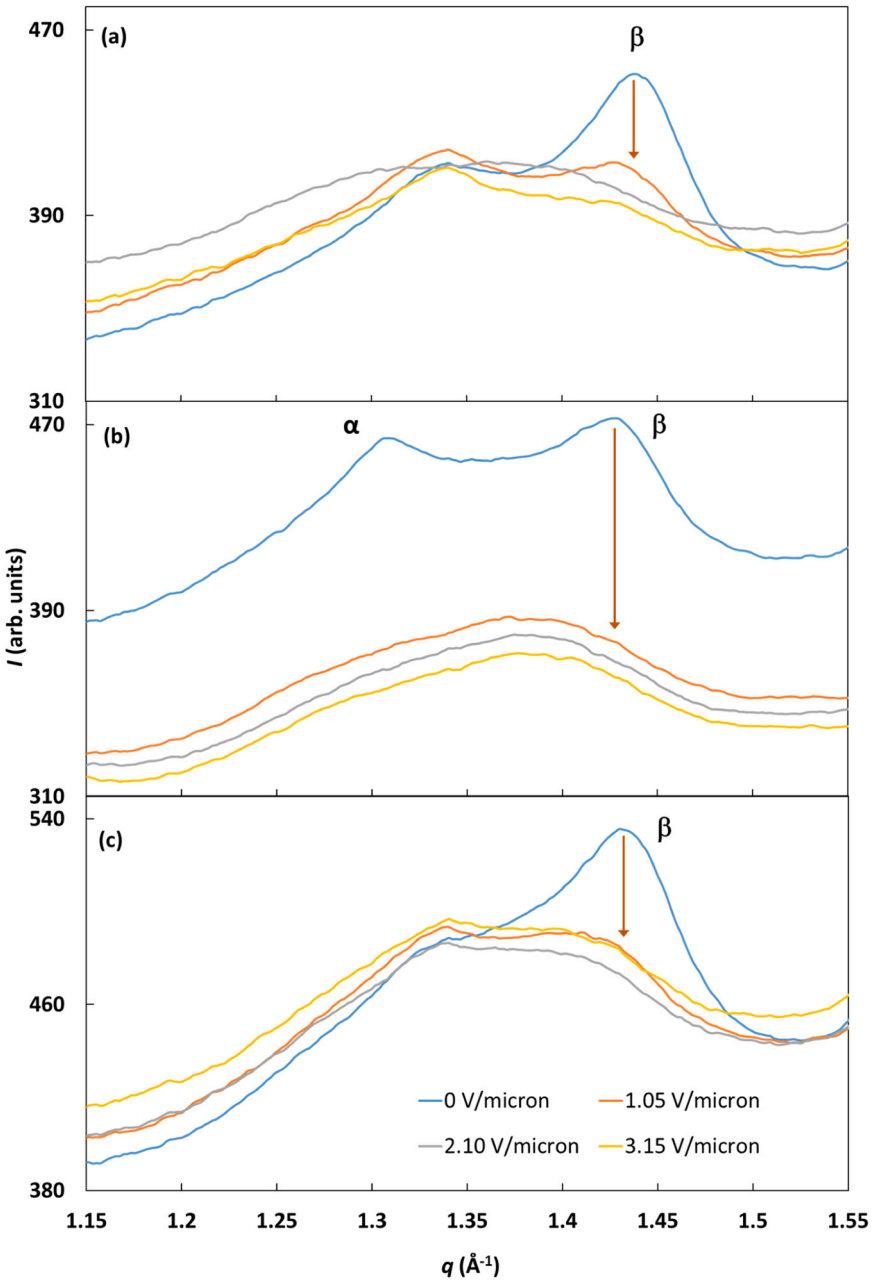

Fig. 3. HRXRD patterns of P(VDF-TrFE) at the middle of the composite film collected at (a) RT, (b) 80 °C, and (c) at the cooled state at different electric fields.

100–130 [29].

The piezoelectric coefficient for pure P(VDF-TrFE) is −30 pC/N, which is larger in absolute value than −22.3 pC/N for P(VDF-TrFE) (70/30) [30] and −24.5 pC/N with dimethyl sulfoxide (DMSO) solvent [31]. Even with a small amount of ceramic particles, the piezoelectric coefficient becomes positive like that of the ceramic, suggesting that the ceramic particles play a key role in the piezoelectric properties. The piezoelectric coefficient becomes 8 pC/N with 60 % $BaTiO_3$. As the piezoelectric coefficient of the composite capacitor increases with the $BaTiO_3$ percentage, the study focusses on a large amount of $BaTiO_3$.

3.2. Overall structure of the composite

As the coercive field E_c is 2.4 V/μm for 60 % $BaTiO_3$ and 2 V/μm for 40 % $BaTiO_3$ [32], operando HRXRD experiments were conducted below E_c at 0 V/μm (Figs. 2a) and 1.05 V/μm, near E_c at 2.10 V/μm, and above E_c at 3.15 V/μm (Fig. 2b) in order to explore the different ferroelectric regimes. The success of the transmission HRXRD experiment with a submicron X-ray beam is a proof of the high quality and planarity of the flexible device with a 2 mm width.

Fig. 2 shows $BaTiO_3$ peaks [28] and α or β P(VDF-TrFE) peaks [33]. Prior to the application of an electric field, the α and β phases are present, whereas no α phase is clearly present in pure P(VDF-TrFE) (Fig. S4). This indicates that the particles favor the crystallization of the α phase. With the application of an electric field, the β peaks disappear, whereas the α peaks remain and an additional α peak even appears. This indicates that the β phase disappears, whereas the α phase is favored. Moreover, some peaks shift from top to bottom and the Full Width Half Maximum (FWHM) of the peaks may evolve as a function of depth, indicating domain size variations. These changes may come from a thermal gradient during annealing on the heating plate or from strains. Later on, these peak modifications are studied in details, on the one hand, for P(VDF-TrFE) and, on the other hand, for $BaTiO_3$.

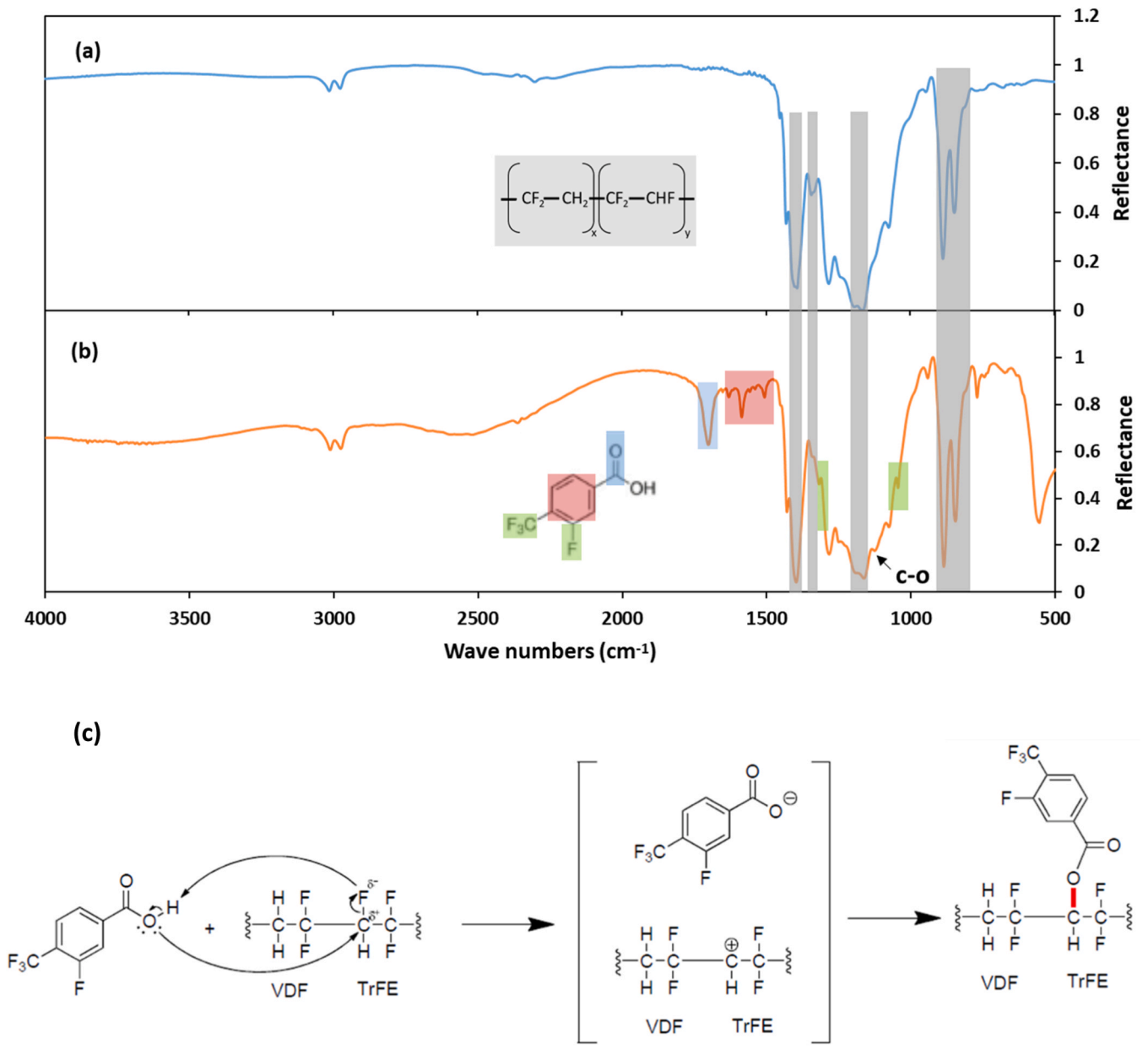

Fig. 4. FTIR reflectance spectra of P(VDF-TrFE) (a) without surfactant, (b) with 10 % of 3 F-met surfactant. (c) proposed interaction between the surfactant and the P(VDF-TrFE).

3.3. Structure of P(VDF-TrFE) in the composite

HRXRD patterns of the P(VDF-TrFE) are displayed in Fig. 3 at the middle of the $BaTiO_3$/P(VDF-TrFE) film (depth = 9.5 μm) at RT, at 80 °C, and at the cooled state at different electric fields.

Prior to the application of an electric field, the FWHM of the β peak is 0.06 $Å^{-1}$ at RT, yielding a domain size of 10 nm, similar to that in pure P(VDF-TrFE) (Fig. S4). The lattice parameters of the β phase are deduced from the HRXRD peaks as a function of the thermal states (Fig. S5). However, the β peak decreases significantly with the application of an electric field as low as ~1 V/μm, indicating unambiguously the quasi-disappearance of the ferroelectric state of P(VDF-TrFE). One possible explanation is that the P(VDF-TrFE) chains form bonds with the surfactant at the surface of the $BaTiO_3$ particles. When an electric field is applied, these bonds may hinder the rotation of P(VDF-TrFE) chains near the particles, leading to a decrease of the crystallinity.

To investigate possible bonds between the P(VDF-TrFE) chains and the surfactant, FTIR experiments were performed on P(VDF-TrFE) in the presence of 10 % surfactant. Previous FTIR spectra of $BaTiO_3$ with the 3 F-met surfactant put in evidence interactions of the surfactant molecules with the particles. The –C═O group of the surfactant disappears to form a $–COO^-$ group [22].

In Fig. 4a, the IR spectrum of the copolymer P(VDF-TrFE) shows characteristic bands that have been reported in literature [34]. These bands include peaks at 842 cm^{-1} associated with $-CF_2$ symmetrical stretching, 880 cm^{-1} associated with $-CF_2$ antisymmetric stretching, and 1400 cm^{-1} associated with $-CH_2$ wagging and CC stretching, indicating the presence of a β-phase crystalline structure. These bands are still present in the IR spectrum of the copolymer with the addition of the 3 F-met surfactant (Fig. 4b), suggesting that the surfactant does not affect the β-phase crystalline structure. Additional significant peaks, attributed to the surfactant, are associated with the $–CF_3$ group at 1050 and 1310 cm^{-1}, –C-C stretching in the benzene ring at 1500 and 1630 cm^{-1}, and a –C═O carbonyl peak at 1700 cm^{-1}. Additionally, a

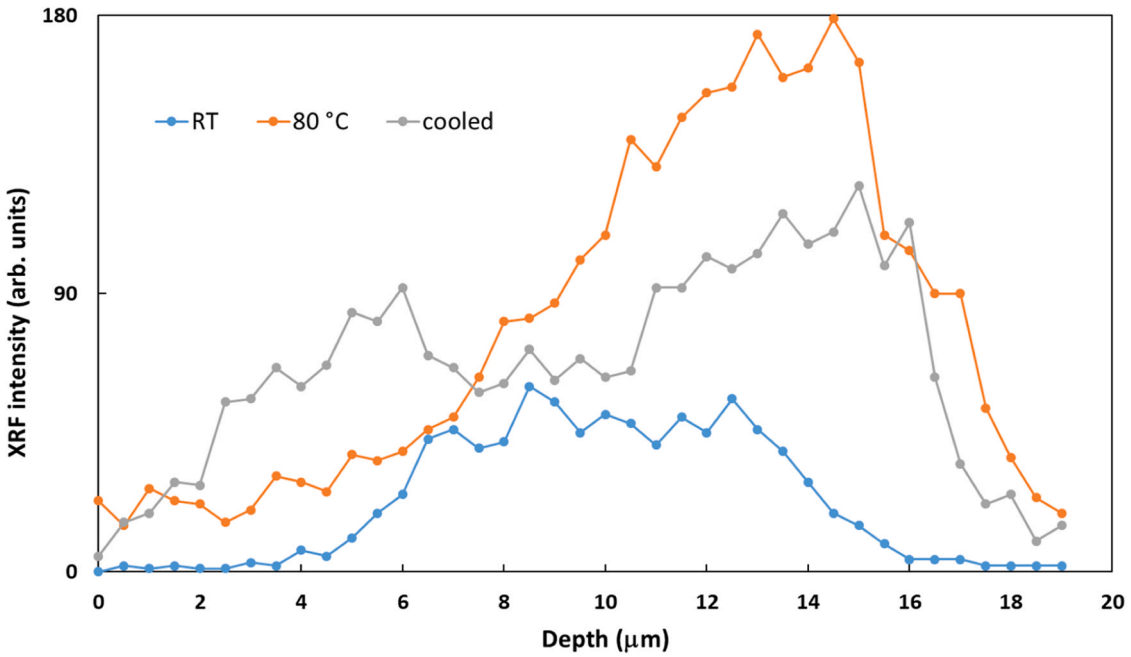

Fig. 5. Fluorescence line intensities of Ba Kα1 as a function of depth at RT, at 80 °C, and at the cooled state.

peak near 1130 cm^{-1} could correspond to the stretching vibration of the C-O group in an ester, suggesting that the surfactant is linked to the copolymer through the formation of an ester functional group. Furthermore, the intensity of the band at 1330 cm^{-1}, which is a marker of TrFE units (-CF stretch), is reduced in the presence of the surfactant, indicating a potential interaction between the TrFE block and the surfactant (Fig. 4c). When the –C═O group of the surfactant is not linked to the particle, this group may be linked to the TrFE block, hindering the rotation of the copolymer during the application of an electric field. When the –C═O group of the surfactant is linked to the particle, it is probable that the hydrophobic regions of the surfactant and P(VDF-TrFE) interact by either hydrophobic bonds or Van der Waals forces. Overall, the functionalization of $BaTiO_3$ with the surfactant implies the quasi-amorphization of the P(VDF-TrFE).

3.4. Structure of the $BaTiO_3$ particles in the P(VDF-TrFE) matrix

As the P(VDF-TrFE) matrix is not ferroelectric during the application of an electric field, it is essential to study the $BaTiO_3$ particles that drive the ferroelectric properties in the composite.

Fig. 5 shows the fluorescence line intensities as a function of depth at RT, 80 °C and at the cooled state.

At RT, the Ba fluorescence profile is well-centered in the matrix film from 6 to 14 μm, i.e. with a FWHM of 8 μm. At 80 °C, the profile drastically shifts by 3 μm towards the bottom. As the temperature of the heating plate increases, the polymer in the bottom layer and the particles in the middle layer diffuse according to Arrhenius law [35]. With the required thermal activation energy, the species can escape their surroundings and move to neighboring environments [36]. Hence, the polymer of the bottom layer and particles of the middle layer are partially transferred in opposite directions leading to mutual diffusion. At the cooled state, Ba is also present in the top of the film and so finally from 2.5 to 16.5 μm, i.e. over 14 μm, nearly twice the initial range. At the end of heating, a similar process occurs between the polymer in the top layer and the underneath particles. This dynamic behavior of the particles is attributed to changes in the viscosity of the polymer at different temperatures, allowing the particles to move more freely. At this state, the percentage of 60 % vol. particles in the second layer is equivalent to 34 % vol. particles in the range where particles are present. Finally due to the 3 F-met surfactant and adequate annealing, the particles are well distributed in the P(VDF-TrFE) film. This clarifies the dependence of the effective permittivity on the distribution of embedded particles [37] and establishes that a homogeneous distribution of particles increases the effective permittivity.

The HRXRD patterns of $BaTiO_3$ exhibit structural changes as function of applied thermal states and electric fields (Fig. 6, Fig. S6, Fig. S7). Splitting of the (002) and (200) peaks has its origin in the tetragonality c/a of $BaTiO_3$. With sufficiently large compressive strains, $BaTiO_3$ has a tetragonal symmetry with polarization parallel to the elongated direction [38]. Upon applied electric field, DWs move in order to maximize domains with polarization parallel to the electric field. Hence, the (002) and (200) peaks evolve as a function of the applied electric field, reflecting the exchange of volume fractions of ferroelectric domains due to the 90° DW motion in perovskite ferroelectrics [39,40]. In contrast, domain switching saturates upon an applied electric field at the cooled state.

The lattice parameters a and c are deduced from the (200) and (002) peak positions in the top and bottom regions at depths of 5 and 14 μm, respectively, as a function of the electric field at different thermal states (Fig. S8). The lattice is larger in the bottom region compared to the top one, due to a thermal gradient during annealing on a heating plate. The average lattice parameters are slightly smaller than the lattice parameters of $BaTiO_3$ particles sintered at 600 °C [41].

Fig. 7 shows the tetragonality c/a at the middle of the top and bottom regions at depths 5 and 14 μm, respectively. The tetragonality is approximately 1.01, in agreement with literature sources [41–44]. More precisely, at 80 °C, the tetragonality is quite small, especially at low electric field. Indeed, the transition from tetragonal to cubic structural phase occurs at 121 °C [45]. Hence, at 80 °C, the tetragonal structure evolves towards the cubic one with c/a=1. On the contrary, at the cooled state and whatever the applied electric field, the tetragonality is even larger than 1.01, due to large strains, leading to improved ferroelectric properties.

The lattice strain S_E during the application of an electric field E is [40]:

$$S_E = (d_E - d_0) / d_0 \quad (3)$$

where d_E and d_0 are the lattice spacing parameters during the

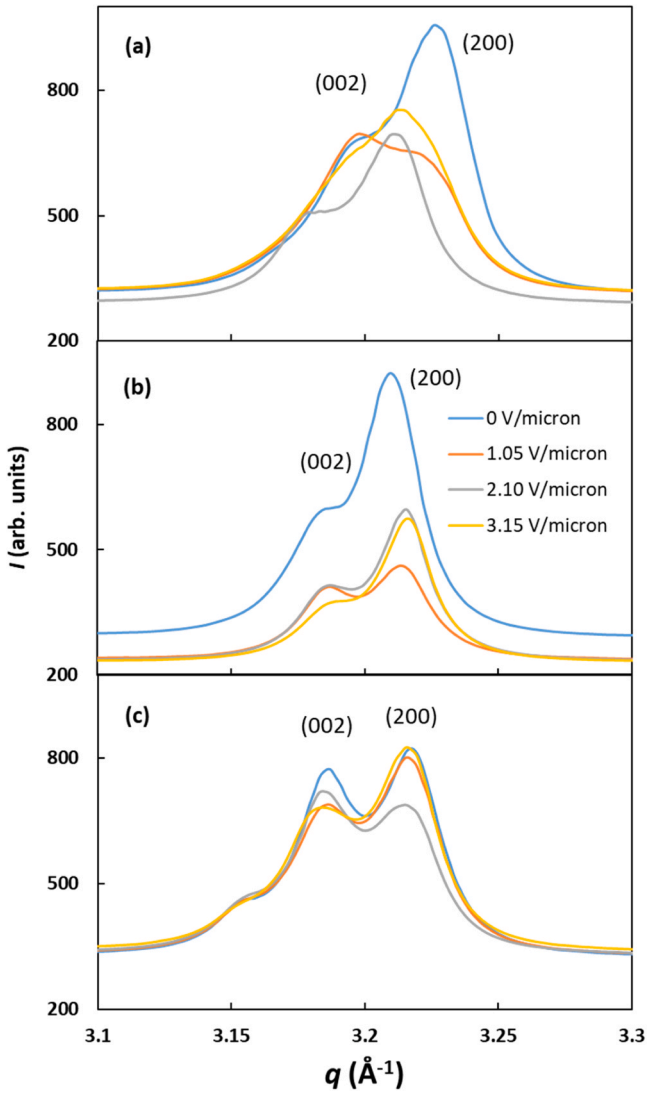

Fig. 6. HRXRD patterns of $BaTiO_3$ at the middle of the composite film recorded at (a) RT, (b) 80 °C, (c) the cooled state at different electric fields.

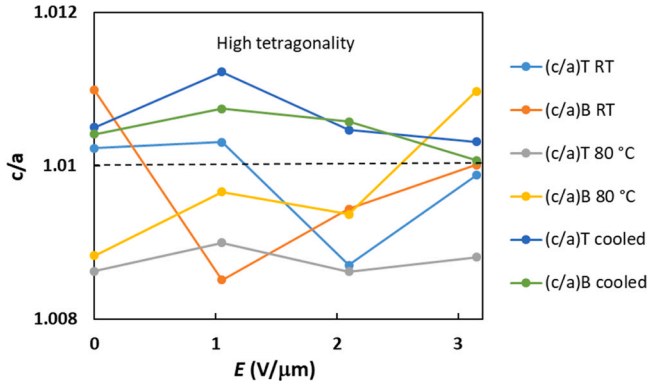

Fig. 7. Tetragonality c/a of $BaTiO_3$ as a function of electric field at RT, at 80 °C, and at the cooled state. T (resp. B) stands for the middle of the top (resp. bottom) of the composite film.

application of an electric field E and at zero field respectively. The lattice strain coefficient $d_{lattice}$ is given by [10]:

$$d_{lattice} = S_E / E \quad (4)$$

The coefficients for (200) and (002), noted d_a and d_c, are displayed in Fig. 8a-c and the domain sizes for (200) and (002), noted Da and Dc, are displayed in Fig. 8d-f as a function of the electric field at different thermal states.

At RT, the lattice strain coefficients and the domain sizes are maximum near E_c. Both parameters evolve similarly, indicating that the lattice strain originates from the motion of DWs and is an extrinsic process. The domain size is in average 20 nm. At 80 °C, it increases to approximately 25 nm, indicating that annealing contributes to the formation of larger domains. The lattice strain coefficients are globally smaller at 80 °C than at RT and evolve quite similarly as the domain size above 1 V/µm, suggesting that the lattice strain is mainly extrinsic. At the cooled state, the increase of the domain size, with respect to the initial state, is to be correlated to the permittivity increase of the composite, confirming the literature [46]. The strain coefficients are approximately zero at E_c and become slightly positive above E_c. The lattice strain coefficient does not evolve systematically as the domain size, suggesting that the lattice strain is mainly intrinsic and corresponds to the spontaneous strain induced by piezoelectric effects. Cooling releases the extrinsic strain due to the motion of DWs, transitioning the strain from extrinsic to intrinsic. The strain coefficient for the c-axis, approximately parallel to E above E_c, corresponds to d_{33} and is equal to 80 pm/V, corresponding to typical d_{33} values of $BaTiO_3$ particles [47]. This intrinsic strain coefficient is nearly 30 times smaller than the extrinsic strain coefficient maximum obtained at the beginning of poling, in agreement with the literature [48]. However, the composite device has a much smaller effective piezoelectric coefficient due to a poor strain transmission from the $BaTiO_3$ particles to the quasi-amorphous P(VDF-TrFE). Improving the transmission of the particle strain in the polymer matrix is crucial to benefit fully from the piezoelectric properties of the ceramic particles.

High-temperature poling not only improves the tetragonality of $BaTiO_3$, but also promotes intrinsic strains and piezoelectric effects.

4. Conclusion

With 60 % vol. $BaTiO_3$ particles initially in the middle layer, the particle distribution becomes successfully homogeneous in P(VDF-TrFE) at the cooled state. After poling at 80 °C, the relative permittivity and the piezoelectric coefficient d_{33} of the composite reach 159 and 8 pC/N respectively. With the application of an electric field, the α phase of P(VDF-TrFE) is still present, whereas the β phase disappears. The study highlights the importance of understanding the interactions between organic and inorganic components in composite materials. The presence of surfactant interactions between the polymer and inorganic particles can significantly affect the material properties, such as the ferroelectric state. By adjusting the surfactant interactions, one may be able to control and enhance the performance of composites for technological applications. This study suggests that other polymers, not ferroelectric, could be used for the matrix in a piezoelectric device. At RT, the lattice strain of the particles is initially extrinsic and becomes intrinsic after annealing and cooling. At the cooled state, the particle tetragonality is larger than 1.01, leading to improved piezoelectric properties. Moreover, the ceramic lattice is compressed in the top region compared to the bottom one. Hence, capacitors annealed on a heating plate may have regions in which properties are enhanced or reduced. At the cooled state, larger particle domains in the whole film lead to greater permittivity. The established relationships facilitate the development of customized flexible piezoelectric composite devices. The combined HRXRD/fluorescence method used in this study can be applied to other devices.

Funding

Part of this work was carried out on the Platform for Nanocharacterization (PFNC) supported by the “Recherche Technologique de Base” and "France 2030 - ANR-22-PEEL-0014" programs of the French

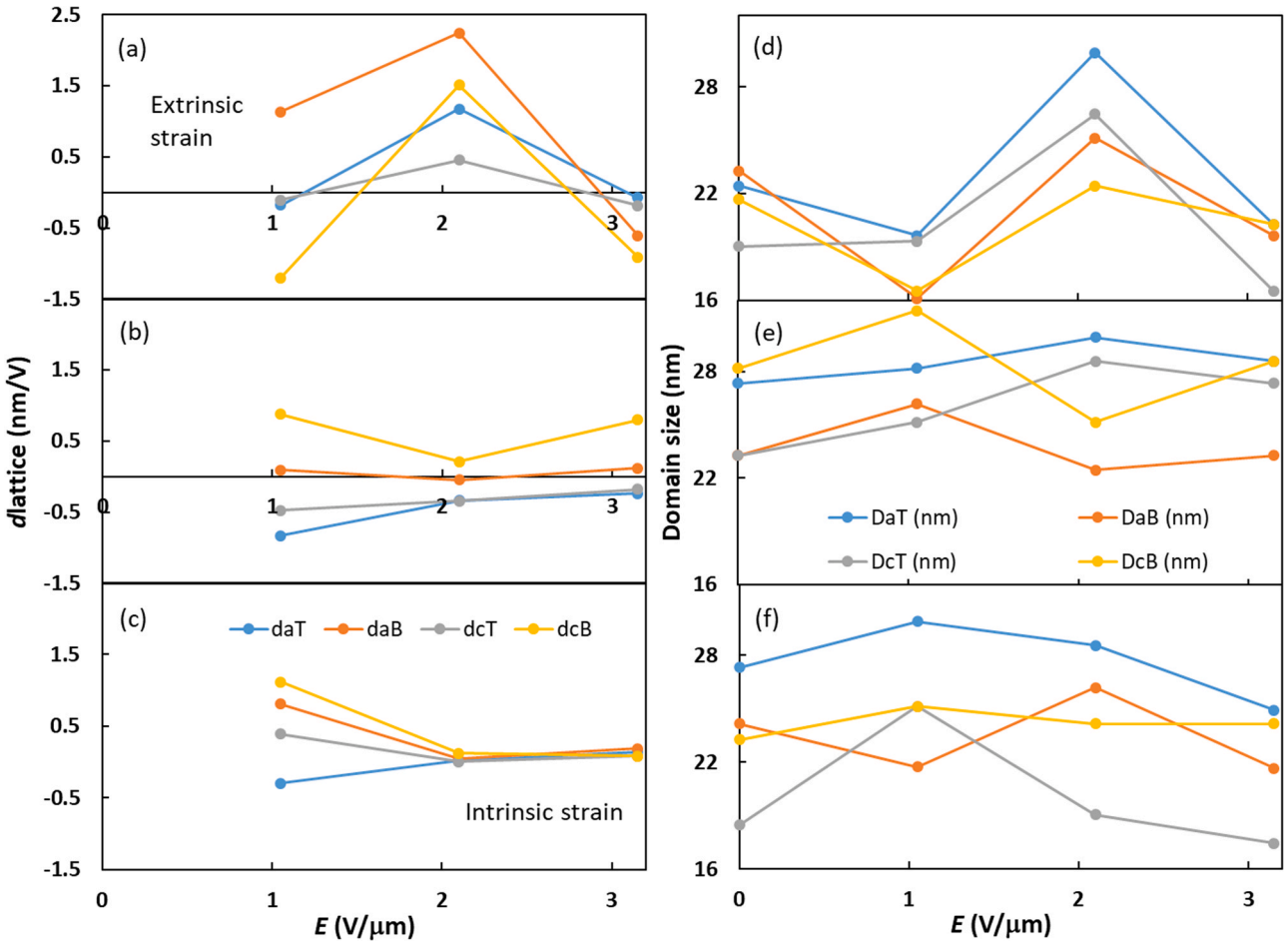

Fig. 8. Lattice strains d_a and d_c (a) at RT, (b) at 80 °C, (c) at the cooled state and average domain size D_a and D_c of $BaTiO_3$ (d) at RT, (e) at 80 °C, (f) at the cooled state as a function of the electric field.

National Research Agency (ANR).

CRediT authorship contribution statement

Mohammed Benwadih: Writing – review & editing, Validation, Resources, Investigation. **Raphaël Ramos:** Writing – review & editing, Validation. **Eleanor Lawrence Bright:** Writing – review & editing, Software, Investigation. **Simon Toinet:** Writing – review & editing, Resources, Investigation. **Sylvain Minot:** Writing – original draft, Visualization, Investigation, Formal analysis. **Christine Revenant:** Writing – original draft, Visualization, Investigation, Formal analysis, Conceptualization.

Declaration of Competing Interest

The authors declare that they have no known competing financial interests or personal relationships that could have appeared to influence the work reported in this paper.

Data Availability

Data will be made available on request.

Acknowledgments

We would like to thank David Alincant for sample preparation. We acknowledge the European Synchrotron Radiation Facility (ESRF) for provision of synchrotron radiation facilities under proposal MA5418. The data is available at https://doi.esrf.fr/10.15151/ESRF-ES-937817538.

Appendix A. Supporting information

Supplementary data associated with this article can be found in the online version at doi:10.1016/j.sna.2024.115738.

References

[1] L. Zhao, Y. Sun, Q. Zhao, Z. Ullah, S. Zhu, M. Zhu, L. Liu, C. Wang, Q. Li, A. He, Y. Wang, F. Ye, Dual-type confinement strategy: improving the stability of organic composite cathodes for lithium-ion batteries with longer lifespan, Chem. Eng. J. vol. 490 (2024) 151547.
[2] R. Chu, H. Song, Z. Ullah, Z. Guan, Y. Zhang, L. Zhao, M. Chen, W. Li, Q. Li, L. Liu, ZIF-8 derived nitrogen-doped carbon composites boost the rate performance of organic cathodes for sodium ion batteries, Electrochim. Acta vol. 362 (2020) 137115.
[3] M. Zheng, Q. Ji, Z. Ullah, Y. Zhang, M. Chen, W. Li, Q. Li, L. Liu, High protection performance based on corrosion media-consumption and barrier properties of the supramolecular polymer reinforced graphene oxide composite coatings, J. Polym. Res. vol. 28 (2021) 426.
[4] N. Abbas, X. Qin, S. Ali, G. Zhu, Z. Yi, X. Yang, X. Zheng, Z. Ullah, K. Gu, J. Tang, Study of microstructural variation with annealing temperature of Ti-Al-C films coated on stainless steel substrates, Int. J. Hydrog. Energy vol. 45 (2020) 3186.
[5] C. Xing, S. Zhu, Z. Ullah, X. Pan, F. Wu, X. Zuo, J. Liu, M. Chen, W. Li, Q. Li, L. Liu, Ultralight and flexible graphene foam coated with Bacillus subtilis as a highly efficient electromagnetic interference shielding film, Appl. Surf. Sci. vol. 491 (2019) 616.
[6] Q. Li, Q. Zeng, L. Gao, Z. Ullah, H. Li, Y. Guo, W. Li, Y. Shi, G. Tao, L. Liu, Self-assembly of urchin-like porphyrin/graphene microspheres for artificial photosynthetic production of formic acid from CO2, J. Mater. Chem. A vol. 5 (2017) 155.

[7] V.-H. Vuong, S.V.N. Pammi, S. Ippili, V. Jella, T.N. Thi, K.S. Pasupuleti, M.-D. Kim, M.J. Jeong, J.-R. Jeong, H.S. Chang, S.-G. Yoon, Flexible, stable, and self-powered photodetectors embedded with chemical vapor deposited lead-free bismuth mixed halide perovskite films, Chem. Eng. J. vol. 458 (2023) 141473.
[8] V.-H. Vuong, S.V.N. Pammi, K.S. Pasupuleti, W. Hu, V.D. Tran, J.S. Jung, M.-D. Kim, V. Pecunia, S.G. Yoon, Engineering chemical vapor deposition for lead-free perovskite-inspired MA3Bi2I9 self-powered photodetectors with high performance and stability, Adv. Opt. Mater. vol. 9 (2021) 2100192.
[9] K.S. Pasupuleti, D. Vidyasagar, L.N. Ambadi, N.-H. Bak, S.-G. Kim, M.-D. Kim, UV light activated g-C3N4 nanoribbons coated surface acoustic wave sensor for high performance sub-ppb level NO2 detection at room temperature, Sens. Actuator B-Chem. vol. 394 (2023) 134471.
[10] M. Acosta, N. Novak, V. Rojas, S. Patel, R. Vaish, J. Koruza, G.A. Rossetti, J. Rödel, BaTiO3-based piezoelectrics: Fundamentals, current status, and perspectives, Appl. Phys. Rev. vol. 4 (2017) 041305.
[11] A. Pramanick, A.D. Prewitt, J.S. Forrester, J.L. Jones, Domains, domain walls and defects in perovskite ferroelectric oxides: a review of present understanding and recent contributions, Crit. Rev. Solid State Mater. Sci. vol. 37 (4) (2012) 243–275.
[12] C.M. Dudhe, S.B. Nagdeote, S.J. Khambadkar, P.R. Arjunwadkar, R.R. Patil, Study of 90° and 180° nanodomains in BaTiO3 nanoparticles using transmission electron microscopy, Ferroelectrics vol. 471 (1) (2014) 148–155.
[13] S. Taleb, M. Badillo, F.J. Flores-Ruiz, M. Acuautla, From synthesis to application: high-quality flexible piezoelectric sensors fabricated from tetragonal BaTiO3/ P (VDF-TrFE) composites, Sens. Actuator A-Phys. vol. 361 (2023) 114585.
[14] V.K. Prateek, Thakur, R.K. Gupta, Recent progress on ferroelectric polymer-based nanocomposites for high energy density capacitors: synthesis, dielectric properties, and future aspects, Chem. Rev. vol. 116 (7) (2016) 4260–4317.
[15] Z. Yao, Z. Song, H. Hao, Z. Yu, M. Cao, S. Zhang, M.T. Lanagan, H. Liu, Homogeneous/inhomogeneous-structured dielectrics and their energy-storage performances, Adv. Mater. vol. 29 (20) (2017) 1601727.
[16] K. Asadi, Organic Ferroelectric Materials and Applications, K. Asadi, Ed., Elsevier, 2022.
[17] G. Arlt, D. Hennings, G. de With, Dielectric properties of fine-grained barium titanate ceramics, J. Appl. Phys. vol. 58 (1985) 1619–1625.
[18] S. Toinet, M. Benwadih, S. Tardif, J. Eymery, C. Revenant, Phase transitions in flexible solution-processed ferroelectric PVDF-TrFE polymer thin films, J. Polym. Res. vol. 29 (2022) 456.
[19] N. Meng, X. Zhu, R. Mao, M.J. Reece, E. Bilotti, Nanoscale interfacial electroactivity in PVDF/PVDF-TrFE blended films with enhanced dielectric and ferroelectric properties, J. Mater. Chem. C. vol. 5 (2017) 3296.
[20] C.K. McGinn, K.A. Kam, M.-M. Laurila, K.L. Montero, M. Mäntysalo, D. Lupo, I. Kymissis, Formulation, printing and poling method for piezoelectric films based on PVDF-TrFE, J. Appl. Phys. vol. 128 (2020) 225304.
[21] T.A. Ali, J. Groten, J. Clade, D. Collin, P. Schäffner, M. Zirkl, A.-M. Coclite, G. Domann, B. Stadlober, Screen-printed ferroelectric P(VDF-TrFE)-co-PbTiO3 and P(VDFTrFE)-co-NaBiTi2O6 nanocomposites for selective temperature and pressure sensing, ACS Appl. Mater. Interfaces vol. 12 (2020) 38614–38625.
[22] C. Carbone, M. Benwadih, G. D'Ambrogio, M.-Q. LE, J.-F. Capsal, P.-J. Cottinet, Influence of matrix and surfactant on piezoelectric and dielectric properties of screen-printed BaTiO3/PVDF composites, Polymers vol. 13 (2021) 2166.
[23] H. Kim, T. Fernando, M. Li, Y. Lin, T.-L.B. Tseng, Fabrication and characterization of 3D printed BaTiO3/PVDF nanocomposites, J. Compos. Mater. vol. 52 (2018) 197.
[24] B. Paci, D. Bailo, V. Rossi Albertini, J. Wright, C. Ferrero, G.D. Spyropoulos, E. Stratakis, E. Kymakis, Spatially-resolved in-situ structural study of organic electronic devices with nanoscale resolution: the plasmonic photovoltaic case study, Adv. Mater. vol. 25 (2013) 4760–4765.
[25] B. Paci, G. Kakavelakis, A. Generosi, J. Wright, C. Ferrero, E. Stratakis, E. Kymakis, Improving stability of organic devices: a time/space resolved structural monitoring approach applied to plasmonic photovoltaics, Sol. Energy Mater. Sol. Cells vol. 159 (2017) 617–624.
[26] A. Aliane, M. Benwadih, B. Bouthinon, R. Coppard, F. Domingues-Dos Santos, A. Daami, Impact of crystallization on ferro-, piezo- and pyro-electric characteristics in thin film P(VDF–TrFE), Org. Electron. vol. 25 (2015) 92.
[27] F. Xu, F. Chu, S. Trolier-McKinstry, Longitudinal piezoelectric coefficient measurement for bulk ceramics and thin films using pneumatic pressure rig, J. Appl. Phys. vol. 86 (1999) 588.
[28] R. Bo, J. Liu, C. Wang, Y. Wang, P. He, Z. Han, Molecular dynamics simulation on structure and dielectric permittivity of BaTiO3/PVDF composites, Adv. Polym. Tech. 9019580 (2021).
[29] S. Dalle Vacche, F. Oliveira, Y. Leterrier, V. Michaud, D. Damjanovic, J.-A. E. Manson, The effect of processing conditions on the morphology, thermomechanical, dielectric, and piezoelectric properties of P(VDF-TrFE)/BaTiO3 composites, J. Mater. Sci. vol. 47 (2012) 4763–4774.
[30] H. Jiang, J. Yang, F. Xu, Q. Wang, W. Liu, Q. Chen, C. Wang, X. Zhang, G. Zhu, VDF-content-guided selection of piezoelectric P(VDF-TrFE) films in sensing and energy harvesting applications, Energy Convers. Manag. vol. 211 (2020) 112771.
[31] J. Kim, J.H. Lee, H. Ryu, J.-H. Lee, U. Khan, H. Kim, S.S. Kwak, S.-W. Kim, High-performance piezoelectric, pyroelectric, and triboelectric nanogenerators based on P(VDF-TrFE) with controlled crystallinity and dipole alignment, Adv. Funct. Mater. vol. 27 (2017) 1700702.
[32] J. Fu, Y. Hou, M. Zheng, Q. Wei, M. Zhu, H. Yan, Improving dielectric properties of PVDF composites by employing surface modified strong polarized BaTiO3 particles derived by molten salt method, ACS Appl. Mater. Interfaces vol. 7 (2015) 24480–24491.
[33] Y. Huang, G. Rui, Q. Li, E. Allahyarov, R. Li, M. Fukuto, G.-J. Zhong, J.-Z. Xu, Z.-M. Li, P.L. Taylor, L. Zhu, Enhanced piezoelectricity from highly polarizable oriented amorphous fractions in biaxially oriented poly(vinylidene fluoride) with pure β crystals, Nat. Comm. vol. 12 (2021) 675.
[34] A. Arrigoni, L. Brambilla, C. Bertarelli, G. Serra, M. Tommasini, C. Castiglioni, P (VDF-TrFE) nanofibers: structure of the ferroelectric and paraelectric phases through IR and Raman spectroscopies, RSC Adv. vol. 10 (2020) 37779.
[35] L. Masaro, X.X. Zhu, Physical models of diffusion for polymer solutions, gels and solids, Prog. Polym. Sci. vol. 24 (1999) 731.
[36] L.-H. Cai, S. Panyukov, M. Rubinstein, Hopping diffusion of nanoparticles in polymer matrices, Macromolecules vol. 48 (2015) 847.
[37] J. Belovickis, M. Ivanov, S. Svirskas, V. Samulionis, J. Banys, A.V. Solnyshkin, S. A. Gavrilov, K.N. Nekludov, V.V. Shvartsman, M.V. Silibin, Dielectric, ferroelectric, and piezoelectric investigation of polymer-based P(VDF-TrFE) composites, Phys. Status Solidi B vol. 255 (2018) 1700196.
[38] Y.L. Li, L.Q. Chen, Temperature-strain phase diagram forBaTiO3 thin films, Appl. Phys. Lett. vol. 88 (2006) 072905.
[39] J.L. Jones, E.B. Slamovich, K.J. Bowman, Domain texture distributions in tetragonal lead zirconate titanate by x-ray and neutron diffraction, J. Appl. Phys. vol. 97 (3) (2005) 034113.
[40] A. Pramanick, D. Damjanovic, J.E. Daniels, J.C. Nino, J.L. Jones, Origins of electro-mechanical coupling in polycrystalline ferroelectrics during subcoercive electrical loading, J. Am. Ceram. Soc. vol. 94 (2) (2011) 293–309.
[41] X. Chen, J. Sun, B. Guo, Y. Wang, S. Yu, W. Wang, Effect of the particle size on the performance of BaTiO3 piezoelectric ceramics produced by additive manufacturing, Ceram. Int. vol. 18 (2023) 1285–1292.
[42] S. Luan, P. Wang, L. Zhang, Y. He, X. Huang, G. Jian, C. Liu, S. Yu, R. Sun, X. Cao, Z. Fu, Atmospherically hydrothermal assisted solid-state reaction synthesis of ultrafine BaTiO3 powder with high tetragonality, J. Electroceram. vol. 50 (2023) 97–111.
[43] P. Yu, W. Liu, P. Gao, T. Shao, S. Zhao, Z. Han, X. Gu, J. Zhang, Y. Wang, Investigation on synthesis of tetragonal BaTiO3 nanopowders by a new wet chemical method, J. Mater. Sci.: Mater. Electron. vol. 33 (2022) 10828–10840.
[44] L. Qi, B.I. Lee, P. Badheka, L.-Q. Wang, P. Gilmour, W.D. Samuels, G.J. Exarhos, Low-temperature paraelectric–ferroelectric phase transformation in hydrothermal BaTiO3 particles, Mater. Lett. vol. 59 (2005) 2794–2798.
[45] V. Mishra, A. Sagdeo, V. Kumar, M.K. Warshi, H.M. Rai, S.K. Saxena, D.R. Roy, V. Mishra, R. Kumar, P.R. Sagdeo, Electronic and optical properties of BaTiO3 across tetragonal to cubic phase transition: An experimental and theoretical investigation, J. Appl. Phys. vol. 122 (2017) 065105.
[46] Q. Li, T. Ju, R. Li, S. Wang, Y. Yang, H. Ishida, Y.-W. Harn, J. Chen, B. Hirt, A. Sehirlioglu, Z. Lin, L. Zhu, Investigation into the crystal structure–dielectric property correlation in barium titanate nanocrystals of different sizes, Nanoscale vol. 15 (2023) 7829.
[47] S. Gaytan, M. Cadena, H. Karim, D. Delfin, Y. Lin, D. Espalin, E. MacDonald, R. Wicker, Fabrication of barium titanate by binder jetting additive manufacturing technology, Ceram. Int. vol. 41 (2015) 6610–6619.
[48] D. Li, J. Barrington, S. James, D. Ayre, M. Sloma, M.-F. Lin, H.Y. Nezhad, Electromagnetic field controlled domain wall displacement for induced strain tailoring in BaTiO3-epoxy, Sci. Rep. vol. 12 (2022) 7504.

Christine Revenant received a PhD in Physics and the habilitation to steer researches ("Habilitation à Diriger des Recherches"), both from the University Grenoble Alpes, France. Her current research interests are focused on the use of laboratory and synchrotron X-ray techniques to explore chemically processed materials for applications in flexible piezoelectric sensors and actuators.

Sylvain Minot is currently a Postdoctoral Fellow at LITEN at CEA Grenoble. He received his PhD in Materials Science from the Institute of Analytical Science in Lyon, France. His research interests include the use and development of physico-chemical techniques for surface characterization, as well as the treatment and functionalization of various materials.

Simon Toinet received the generalist engineering degree from ECAM Lyon in 2021. Now, he is a Ph.D. candidate at INSA Lyon (France). His research interests include piezoelectric materials, flexible electronics, organic electronics, multi-layer actuators and innovative medical devices.

Eleanor Lawrence Bright is currently a beamline scientist focused on x-ray diffraction techniques at the Rossendorf Beamline (BM20) at the European Synchrotron Radiation Facility (ESRF), part of the Helmholtz-Zentrum Dresden-Rossendorf. She previously worked as a Post-Doc on the ID11 beamline at ESRF after completing a PhD in Physics at the University of Bristol, UK.

Raphael Ramos received a PhD degree in physics in 2008 from Grenoble University, France. He worked as a research fellow at the University of California in Santa Barbara from 2008 to 2011. His research interests revolve around the advanced characterization of materials and processes for electronics and energy applications, with a specific focus on the optical spectroscopy of energy-related materials.

Mohammed Benwadih received a Ph.D. degree in Micro and nanotechnology from Lille 1 in 2014. He is currently a researcher in flexible electronics unit in CEA. His research

interests are the use and development of materials for flexible application, as well as the fabrication of films and components.